The Astrophysical Journal Letters, 915:L19 (8pp), 2021 July 1 https://doi.org/10.3847/2041-8213/ac0aee

Direct Evidence for Magnetic Reflection of Heavy Ions from High Mach Number Collisionless Shocks

Hadi Madanian[1], Steven J. Schwartz[2], Stephen A. Fuselier[1,3], David Burgess[4], Drew L. Turner[5], Li-Jen Chen[6], Mihir I. Desai[1,3], and Michael J. Starkey[1]
[1] Southwest Research Institute, 6220 Culebra Road, San Antonio, TX 78238, USA; hmadanian@gmail.com
[2] Laboratory for Atmospheric and Space Physics, University of Colorado, Boulder, CO 80303, USA
[3] University of Texas at San Antonio, San Antonio, TX 78249, USA
[4] Queen Mary University of London, London, UK
[5] Johns Hopkins University Applied Physics Laboratory, Laurel, MD 20723, USA
[6] NASA Goddard Space Flight Center, Greenbelt, MD 20771, USA
Received 2021 May 6; revised 2021 June 10; accepted 2021 June 11; published 2021 July 2

Abstract

Strong shocks in collisionless plasmas, such as supernovae shocks and shocks driven by coronal mass ejections, are known to be a primary source of energetic particles. Due to their different mass per charge ratio, the interaction of heavy ions with the shock layer differs from that of protons, and injection of these ions into acceleration processes is a challenge. Here we show the first direct observational evidence of magnetic reflection of alpha particles from a high Mach number quasi-perpendicular shock using in situ spacecraft measurements. The intense magnetic amplification at the shock front associated with nonstationarity modulates the trajectory of alpha particles, some of which travel back upstream as they gyrate in the enhanced magnetic field and experience further acceleration in the upstream region. Our results in particular highlight the important role of high magnetic amplification in seeding heavy ions into the energization processes at nonstationary reforming shocks.

Unified Astronomy Thesaurus concepts: Shocks (2086); Space plasmas (1544); Solar wind (1534)

1. Introduction

Fast-moving collisionless shocks in space and astrophysical plasmas are regions of wave-particle interaction, energy transfer, and generation of highly energetic ions. Particle energization occurs through different acceleration processes, some of which become effective when seed ions obtain a minimum energy to engage in the process (Caprioli et al. 2015; Marcowith et al. 2020). The mechanisms by which ions from the bulk or thermal plasma are pre-accelerated to seed the acceleration process has been a point of debate (Marcowith et al. 2016). Seeding and energization of heavy ions are of particular interest. Analysis of emission spectra from astrophysical shocks has shown mass-per-charge dependent preferential heating of heavy ions occurs in the post shock plasma (Miceli et al. 2019). In addition, abundance enhancement of heavy ions in galactic cosmic rays are believed to be caused by their acceleration at astrophysical shocks, and several modeling studies have been able to adapt mass-dependent injection schemes to accelerate ions from a thermal ion pool (Eichler & Hainebach 1981; Caprioli et al. 2017). At high Mach number shocks, part of the upstream bulk flow energy is dissipated by the cross-shock electrostatic potential through ion reflection (Hudson & Kahn 1965; Paschmann et al. 1982). Ions with a kinetic energy less than this potential will be reflected back upstream, while directly transmitted ions are decelerated. Depending on their trajectory, reflected ions can be accelerated by the motional electric field ($\boldsymbol{E} = -\boldsymbol{V} \times \boldsymbol{B}$) or by the electric field within upstream perturbations. Reflected ions can also cause high-amplitude magnetic enhancements in the upstream region that lead to nonstationarity and quasi-periodic reformation of the shock front (Hellinger et al. 2002; Bell 2004; Caprioli & Spitkovsky 2014a; Burgess et al. 2016). Reforming shocks in general exhibit a more intense magnetic amplification at the shock front (Russell et al. 1982; Sulaiman et al. 2015; Madanian et al. 2021). Such strong fields can have an influence on the trajectory and the subsequent acceleration efficiency of upstream ions (Giacalone et al. 1991; Caprioli & Spitkovsky 2014b).

The plasma of interplanetary shocks and planetary bow shocks is dominated by protons. Alpha particles constitute the most abundant minor heavy ion species with typical densities less than five percent of the proton density (Kasper et al. 2007). Due to their different mass per charge ratio, alpha particles experience a weaker deceleration by the cross shock electrostatic potential relative to protons (Gedalin 2020a). Since the potential self-adjusts to process the main proton component, it is insufficient to reflect alpha particles. Directly transmitted alpha particles farther downstream of the shock form a ring beam distribution, which is unstable in the background drifting proton plasma and become isotropized into a shell-like distribution (Fuselier et al. 1988). On the other hand, several studies have reported on the presence of nonthermal alpha particles upstream of Earth's bow shock (Ipavich et al. 1984; Fuselier et al. 1990, 1995; Broll et al. 2018). It was initially thought that ion leakage from the heated plasma in the downstream region produces these ions. However, later investigations that compared He^{2+}/H^{+} density ratios in the energized and thermal ion populations determined that these ions originate from the solar wind.

To date, there have been no direct measurements to bridge the knowledge gap on how heavy ions reflect at high Mach number shocks. In what follows, we show direct observational evidence for magnetic reflection of alpha particles at high Mach number quasi-perpendicular shocks using high-resolution in situ spacecraft observations.

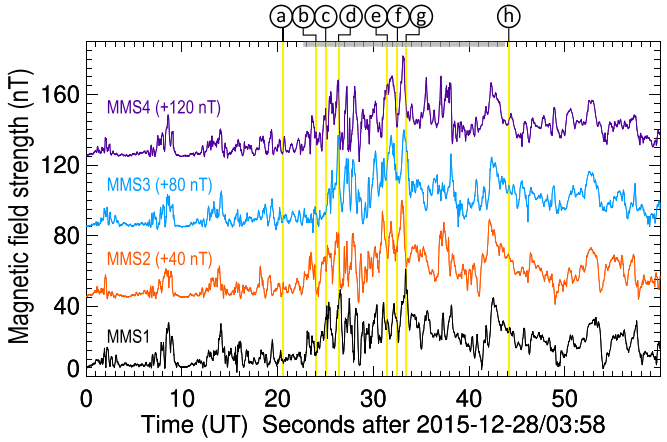

Figure 1. Nonstationarity and magnetic amplification. Magnetic field profiles measured by four MMS spacecraft between 03:58:00 and 03:59:00 UT on 2015 December 28. The spacecraft have a close tetrahedron formation traveling near the orbit apogee. Data from MMS2 (orange), MMS3 (blue), and MMS4 (purple) are shifted in magnitude by 40, 80, and 120 nT, respectively, to avoid clutter. The gray bar on the top marks the main shock transition period. Several timestamps are highlighted on this figure for further analysis of underlying ion distributions.

2. Data Sets

We use in situ measurements from the Magnetospheric MultiScale (MMS) spacecraft (Burch et al. 2016). Ultra high time resolution of MMS observations at Earth's bow shock have enabled studying new interesting microphysical shock processes. In our analysis, magnetic field vectors are from the fluxgate magnetometer (Russell et al. 2016), electric field data from the electric double probe (EDP) experiment (Ergun et al. 2016; Lindqvist et al. 2016), and 3D ion measurements from two separate instruments: the fast plasma investigation (FPI) instrument (Pollock et al. 2016), and the hot plasma composition analyzer (HPCA; Young et al. 2016). The FPI ion measurement cycle is 150 milliseconds with no mass-per-charge differentiation. The HPCA obtains distributions of five major ion species every 10 s. We use HPCA data to confirm the presence of reflected alpha particles, while FPI data provide the necessary tool to investigate detailed microphysics of the reflection processes. Although the FPI does not distinguish between ion species, signatures of cold ion populations for both protons and alpha particles can be distinguished in the distribution. Since protons and alpha particles move together in the solar wind flow, they are expected to have a similar trace and trajectory in the velocity space. However, due to their different mass per charge ratios, their associated beams appear at two separate energies in the FPI electrostatic analyzer, and at separate velocities in the velocity space. The FPI also measures the electron pressure tensor which we use to obtain the ambipolar electric field. The results in this Letter are based on satellite 1 (MMS1) measurements, except spatial derivatives for which all four spacecraft data are utilized.

3. Observations and Results

Figure 1 shows four MMS spacecraft observations of the magnetic field during a transition from the upstream solar wind to the downstream magnetosheath. The main shock transition layer, corresponding to the period of high magnetic fluctuations in data, is marked with a gray bar. Although the intra-spacecraft separation between different MMS pairs is on average only 25 km, each spacecraft sees a different shock profile, indicative of the spatial and time-varying nature of the shock layer. The magnetic field far upstream in the unperturbed solar wind is about 2.7 nT, while the highest magnetic field strength at the shock is 60.5 nT. The upstream plasma density is 10.5 cm^{-3} while the alpha particle to proton density ratio is 0.04. The shock has a quasi-perpendicular orientation ($\theta_{Bn} = 83°$) and travels in the upstream solar wind flow with an Alfvénic Mach number of $M_{\rm Alf} = 27$. While such a Mach number is relatively high for planetary bow shocks, it is considered fairly low in astrophysical shock studies. An earlier analysis of this shock event described its nonstationarity and reforming nature (Madanian et al. 2021). It was shown that reflected protons generate magnetic enhancements in the upstream region that are convected toward the shock by the solar wind. They cause significant variation and intense magnetic amplification in the shock layer.

Figure 2 shows ion velocity distributions at several instances across the shock as measured by the FPI. The top row distributions are in the normal incidence frame (NIF) with the abscissa along $\hat{n}$ and the ordinate along the upstream motional electric field $\hat{e}$. Figure 2(a) shows an ion distribution upstream of the shock, where the solar wind proton beam is labeled at $V_n \sim -350\,{\rm km\,s^{-1}}$. The arc-shaped feature in the distribution that begins at $V_n \sim 200\,{\rm km\,s^{-1}}$ represents shock reflected solar wind protons and includes freshly reflected ions traveling Sunward ($V_n > 0$, $V_e \sim 0$), ions being turned around by the motional electric field ($V_n \sim 0$, $V_e > 0$), and reflected ions that are further accelerated and are returning to the shock with $-V_n$ velocity component (RR ions). The distribution in Figure 2(b) is near the upstream edge of the shock transition layer. The solar wind alpha particle beam is identified at $V_n \sim -500\,{\rm km\,s^{-1}}$. An interesting ion feature in Figure 2(c) is a population of reflected ions at higher velocities than protons, which we associate with alpha particles. Small traces of reflected alpha particles are also observed in Figures 2(a), (b) (marked with red arrows). The flux intensity of these ions progressively increases into the shock layer. In Figure 2(d) we show that adjusting the mass-per-charge ratio of an ion at those velocities for an alpha particle results in a velocity trace similar to that of protons. The higher rigidity of alpha particles may allow them to experience a larger potential difference along the motional electric field. We select a number of points, where the two arcs in the velocity space are well distinguishable, marked by red diamonds. We transform these velocities to the energy space through the proton NIF, and remap the resultant energies back to the velocity space with the mass per charge ratio of an alpha particle. The results, marked with black triangles, fall along the same path as protons, though at slightly higher speeds. This agreement supports our claim that ions observed at higher speeds are indeed alpha particles that are processed as protons by the FPI. It should be noted that the NIF transformation also affects alpha particles differently than protons, which can contribute to the different speed of the alpha particle trace. These observations also agree with the HPCA measurements of He^{2+} ions acquired over a longer time period (see Figure C2 in the Appendix), confirming our interpretation of these features.

Comparison of reflected ion populations in Figures 2(a)–(d) reveals interesting differences between reflection of protons versus alpha particles. Nearly specular reflection of protons by the cross-shock electrostatic potential creates an ion signature

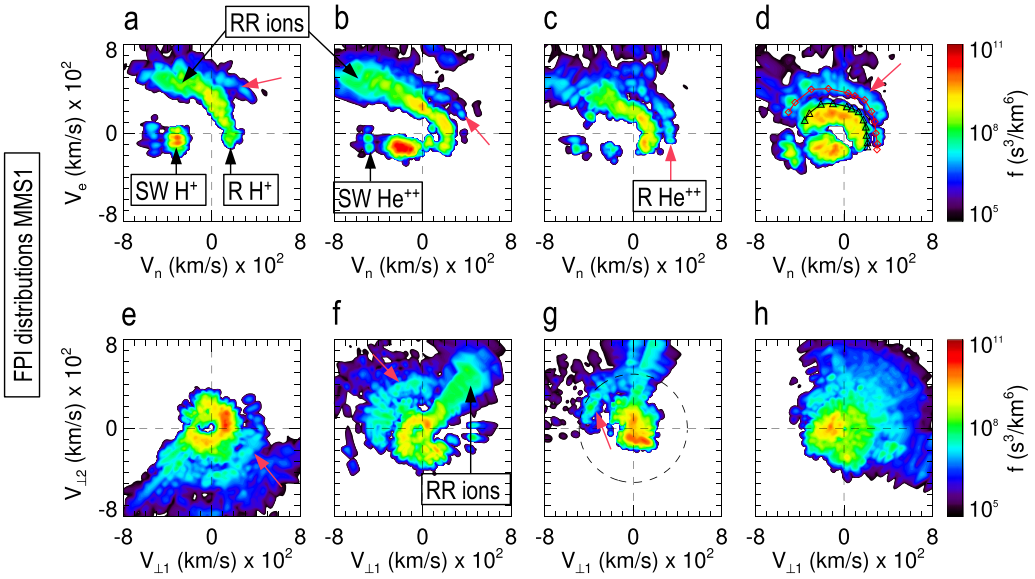

Figure 2. Evidence of alpha particle reflection. This figure shows ion phase space density ($s^3\ km^{-6}$) distributions across the shock. Each distribution shows FPI data over a single measurement cycle. The corresponding timestamps are indicated in Figure 1 with lowercase letters. Distributions in panels (a)–(d) are shown in the NIF in a plane containing $\hat{n}$ and the upstream motional electric field $\hat{e}$. The third coordinate axis in this system is into the page, tangent to the shock surface, and along the projection of the upstream magnetic field. Distributions in panels (e)–(h) are shown in the local plasma frame in a plane perpendicular to the magnetic field. Ion populations of protons (H^+) and alpha particles (He^{2+}) are identified by SW (solar wind), R (reflected), and RR (returning reflected) labels. Red arrows indicate populations of non-gyrotropic alpha particles.

with reversed V_n velocity of the incident solar wind protons, as shown in Figures 2(a)–(c), which are associated with newly reflected ions. Reflected alpha particles in Figures 2(a), (b) lack such an ion population and seem to be further along in their cycloidal motion. The ion populations in Figure 2(d) are also rather distinct compared to previous upstream distributions in that, the energization of returning ions along the upstream motional electric field is lessened or diminished. Alpha particles exhibit non-gyrotropic distributions and appear in gyration in the enhanced magnetic field environment. Depending on their gyrophase and the dynamically variable background magnetic field topology, they can appear upstream of the shock. These observations are a direct indication that the trajectory of alpha particles and their reflection from the shock are driven by magnetic forces at the shock front. The dominance of gyrokinetic effects is supported by the intense magnetic amplification in this region. The corresponding magnetic field strength for distributions in Figures 2(a)–(d) is 9.8, 12.4, 29.2, and 36.9 nT, respectively corresponding to a magnetic enhancement ratio of 3.7, 4.6, 11, and 13.9 from the upstream condition. However, it should also be noted that Figure 1 shows that at timestamp (d), MMS3, which is 20 km behind MMS1 along the shock normal, is observing a significantly larger magnetic field of ∼57 nT.

Gyrating alpha particles that are not reflected eventually propagate downstream. Figure 2(e)–(g) shows ion distributions deeper in the shock layer in a plane perpendicular to the local magnetic field. Noteworthy in these distributions is the non-gyrotropic alpha particle population denoted by red arrows, consistently observed at $|V| \sim 400\ km\ s^{-1}$. Figure 2(e) also shows a population of dispersed energetic ions in the lower half of the plane. A possible source for these ions could be returning reflected ions that have been scattered by the shock or upstream structures. In Figure 2(e) and (f), the intense ion fluxes around the origin occupying almost all four quadrants of the velocity space are directly transmitted protons, which seem to be driven locally at the shock front (i.e., no acceleration comparable to the upstream motional electric field). The streak of ions in the $(+V_{\perp 1},\ +V_{\perp 2})$ quadrant in Figure 2(f) also shows the returning reflected ions accelerated to different energies and in propagation toward downstream. The gyrophase range of alpha particles between Figure 2(e) and (f) changes due to a rotation in the local magnetic field direction. We also note that the magnetic field at times (c), (d), (f), and (g) timestamps also has a substantial component perpendicular to the coplanarity plane. The distribution in Figure 2(g) is measured at the highest magnetic field strength across the shock, as measured by MMS1. It shows an almost isotropic population of protons, a non-gyrotropic population of alpha particles, and returning reflected ions. The distribution in Figure 2(h) is measured near the downstream edge of the shock transition layer showing an example of the fully shocked solar wind plasma where ions exhibit a filled-shell distribution.

The consistent presence of gyrating alpha particles with relatively constant gyration speeds across the shock, as shown in Figure 2(e)–(g), indicates that heavy ions are less sensitive to the cross-shock potential than protons (Gedalin 2020a; Fuselier & Schmidt 1994). Alpha particles are also less likely to be scattered by waves at the shock, which are excited predominantly at proton kinetic scales. In fact, analysis of the electric field across the shock between 03:58:20–40 UT reveals that the normal component of the field changes constantly without an obvious nonzero trend, indicative of a continuous buildup of a potential (Figure 3). It is unclear how a cross-shock electrostatic potential varies at a nonstationary shock, since incident upstream perturbations can maintain a variable fraction of that potential. Therefore, it is difficult to infer a potential for these shocks through conventional methods. Nonetheless, the rate of change in the proton kinetic energy can be used as a proxy to estimate an "effective" cross-shock potential, and to determine its effect on the alpha particle beam (see Appendix B). The upstream proton flow for this event has a speed of

Table 1
Plasma, Shock, and Scale Parameters for Three Events

Date/Time	$M_{\rm Alf}$	$M_{\rm fm}$	θ_{Bn} (Deg.)	$B_{\rm up}$ (nT)	$R_{\rm Max}$	B_d (nT)	$V_{\rm up,\ NIF}$ (km s^{-1})	$V_{\rm dn}$ (km s^{-1})	V_α (km s^{-1})	L (km)	ρ_α (km) [nT]
2015Dec28/03:58:24	27.0	15.0	83	2.7	22.4	15.2	474.1	108.7	343.4	325.6	229.0 [31.3]
2015Dec28/04:32:04	20.1	12.8	68	3.0	19.2	12.6	472.8	99.6	341.6	391.7	233.1 [30.6]
2018Dec16/01:23:32	24.0	4.9	76	0.7	20.1	3.7	223.1	54.8	162.8	629.4	399.9 [8.5]

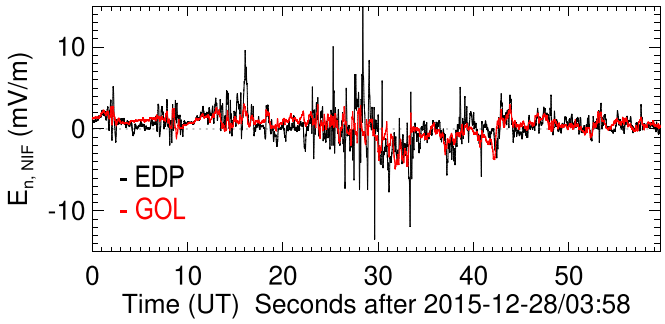

Figure 3. Electric field variations across the shock. The electric field component along the shock normal vector obtained from two sources: 1) from the EDP measurements on board MMS1 (black), and 2) from the direct calculation of the Generalized Ohm's Law (GOL) using four spacecraft measurements (red). The two estimates overall are in good agreement except when spiky features in EDP data are present.

$V_{\rm up,NIF} = 474.1$ km s^{-1} in the NIF, and observations downstream of the shock indicate an asymptotic flow speed of $V_{\rm dn} = 108.7$ km s^{-1} along the shock normal. The associated shock potential would decelerate alpha particles to $V_\alpha = 343.4$ km s^{-1}, which is mostly the gyration speed. This speed in the FPI frame is marked with the dashed circle in Figure 2(g), where our estimate from this simple approach seems to agree reasonably well with the gyration speed of the observed nongyrotropic alpha particles.

4. Discussion and Conclusions

By using high time resolution in situ spacecraft measurements we investigate the physical mechanism behind reflection of alpha particles from high Mach number quasi-perpendicular shocks. Detailed analysis of a case study shows that the shock is highly nonstationary and is dynamically modified by upstream transient perturbations. The highest magnetic amplification ($R_{\rm Max}$) at the shock reaches more than 22 times the upstream magnetic field strength. In Figure 1 we show that such an intense magnetic amplification is accompanied by upstream magnetic perturbation, which is generated by ion kinetic processes and further amplified at the shock (Caprioli & Spitkovsky 2014a; Sulaiman et al. 2015; Sundberg et al. 2017; Madanian et al. 2021). Our detailed analysis of ion distributions in Figure 2, upstream, within, and immediately downstream of the shock indicates that alpha particles create vortices in the velocity space as they gyrate in the enhanced magnetic field at the shock front. Depending on their gyrophase and the background magnetic field topology, some gyrating alpha particles travel upstream of the shock as reflected ions.

Extreme magnetic amplification at the shock front, much stronger than both upstream and downstream magnetic fields, is essential for the magnetic reflection process. In the stationary regime, the shock transition scale (L) is on the order of the upstream proton convective gyroradius in the downstream magnetic field (Bale et al. 2003). Therefore, the shock appears as a discontinuity to heavy ions (Gedalin 2020b). However, for the nonstationary shock considered here, the convective gyroradius of decelerated alpha particles in the intense magnetic field of the shock front (ρ_α) is much smaller than the shock transition scale (Table 1), which allows for effective gyromotion of alpha particles in that region. We also identify this behavior in two other shock events listed in Table 1. For these shocks we observe the following: 1) shock front nonstationarity and high magnetic amplification rates, 2) reflected alpha particles upstream of the shock in HPCA data, and 3) signatures of non-gyrotropic alpha particle distributions at the shock front in FPI data. The relation between different scale parameters as discussed above is valid also for these shocks, which support our interpretation of the magnetic reflection process through these observations. The value inside the bracket in the last column of Table 1 is the magnetic field used to calculate ρ_α, taken at the center of the MMS tetrahedron and averaged over the compression region observed close to the shock front.

The shock events in this study have a quasi-perpendicular orientation. However, at quasi-parallel shocks steepening of upstream ultra-low frequency waves also creates large amplitude magnetic pulsations and intense magnetic amplification at the shock front (Schwartz & Burgess 1991; Burgess & Scholer 2013; Liu et al. 2021), which suggests that magnetic reflection can also function at quasi-parallel shocks. Interestingly, several previous studies that report on the presence of reflected alpha particles upstream of the terrestrial bow shock have also been conducted at shocks that show noticeably high magnetic amplification and nonstationary features (Fuselier et al. 1990; Broll et al. 2018), although these effects were unrecognized or overlooked in those studies.

We report on the first observational study that provides rationale for reflection of heavier-than-proton ions at collisionless shocks in proton-dominated plasmas. Is is argued that, unlike protons, alpha particles are reflected through gyration in the dynamically intensified magnetic field at the shock front. Since reflected ions seed the diffused ion population, our findings suggest that shocks that exhibit high magnetic amplification (i.e., reforming shocks at high Mach numbers) are more likely to produce a diverse admixture of heavy ion species and protons in the diffused energetic ion population. These observations have important implications for theoretical and simulation studies of heavy ion acceleration at high Mach number astrophysical shocks (Caprioli et al. 2017, 2011; Meyer et al. 1997), generation of heavy solar energetic particles (Yang et al. 2011), and heavy ion interactions with plasma structures inside the solar corona (Zimbardo 2011).

This work was supported in part by National Aeronautics and Space Administration (NASA) grants NNG04EB99C and 80NSSC18K1366. All data used in this study are hosted by

NASA and are publicly accessible at (https://spdf.gsfc.nasa.gov/pub/data/mms). We thank the entire MMS team for providing the mission data.

Appendix A
Electric Field across the Shock

The electric field (shown in Figure 3) can be calculated from the electron equation of motion and the Generalized Ohm's Law (GOL):

$$\boldsymbol{E}_{\rm GOL} = -\boldsymbol{v}_e \times \boldsymbol{B} + \frac{1}{en_e}\nabla.\boldsymbol{P}_e + \boldsymbol{V}_{\rm NIF} \times \boldsymbol{B} \tag{A1}$$

where $\boldsymbol{v}_e$, n_e, and $\boldsymbol{P}_e$ are the electron velocity, density, and pressure tensor, respectively, and e is the unit charge. The last term in Equation (A1) is the transformation field into the NIF. $\boldsymbol{V}_{\rm NIF}$ is defined by $\boldsymbol{V}_{\rm NIF} = \hat{n} \times (\boldsymbol{V}_{\rm SW,shock} \times \hat{n})$, where $\boldsymbol{V}_{\rm SW,shock}$ is the upstream solar wind velocity in the shock rest frame. We directly estimate the right-hand side of Equation (A1) using measured quantities. $\boldsymbol{v}_e$, n_e, and $\boldsymbol{B}$ are interpolated to the center of the MMS tetrahedron. The divergence term in Equation (A1) is the ambipolar field and is calculated using electron pressure tensors and spatial derivative techniques for multipoint measurements (Chanteur 1998). The off-diagonal terms in the electron pressure tensors are assumed to be small and negligible. Inertial terms in the GOL are also ignored.

The electric field is also measured directly on board by the EDP instrument. A low bandpass filter has been applied to electric field data to remove variations higher than 12 Hz, matching the electron sampling rate, before calculating the normal component. Ideally, the cross-shock electrostatic potential can be obtained by integrating the normal component of the electric field E_n in the de Hoffman–Teller (dHT) frame (De Hoffmann & Teller 1950), in which the upstream solar wind flow velocity becomes parallel to the upstream magnetic field. However, for highly oblique quasi-perpendicular shocks, the electric field in the dHT frame is completely dominated by the transformation field and the shock potential cannot be determined through conventional methods (Schwartz et al. 2021). In addition, the speed of the shock front at nonstationary reforming shocks is modualted by upstream cyclic perturbations, further complicating the spatial integration of the electric field.

Appendix B
Ion Motion in the Downstream

We adopt a simple approach to determine the dominant velocity component of heavy ions at the shock front. The rate of change in the proton kinetic energy along the shock normal provides an estimate of the effective cross-shock electrostatic potential (Lee & Wu 2000; Gedalin 2020a), which can be obtained from

$$e\Delta\Phi = \frac{1}{2}m_p(V_{\rm up}^2 - V_{\rm dn}^2) \tag{B2}$$

where m_p is the proton mass, and $V_{\rm up}$ and $V_{\rm dn}$ are the upstream and downstream proton flow speeds along the shock normal, respectively. It is assumed that velocity variations due to $\Delta\Phi$ for all ions is along $\hat{n}$ (i.e., $V_{\rm up}\tan(\theta_{Bn}) = V_{\rm dn}\tan(\theta_{\rm dn})$, where $\theta_{\rm dn}$ is the downstream obliquity angle). We define ϵ as the ratio of the cross-shock electrostatic potential to the upstream proton kinetic energy. From B2, the downstream velocity of incident ion i with mass M and charge state Q is defined as

$$V_{{\rm dn},i} = V_{\rm up}(1 - \epsilon\, Q/M)^{1/2} = \alpha V_{\rm up} \tag{B3}$$

In the dHT frame, the ion gyration speed ($V_{{\rm dn},\ g}$) and the variation in the field-aliened velocity component ($\Delta V_{{\rm dn},\|}$) immediately downstream of the shock are determined by the downstream velocity difference between the ion and the proton flow (ΔV_i) through

$$\Delta V_i = V_{{\rm dn},i} - V_{\rm dn} = V_{\rm up}\left(\alpha - \frac{B_{\rm up,tang.}}{B_{\rm dn,tang.}}\right) \tag{B4}$$

$$(\Delta V_{{\rm dn},\|},\, V_{{\rm dn},g}) = \Delta V_i(\cos(\theta_{\rm dn}),\, \sin(\theta_{\rm dn})) \tag{B5}$$

In these equations, tang. and n subscripts refer to the total tangential and normal components of the magnetic field. Equation (B5) indicates that immediately downstream of high Mach number quasi-perpendicular shocks where $\theta_{\rm dn} \to 90°$, the ion motion is dominated by gyration. For shocks with high magnetic amplification, Equation (B5) may be rewritten as

$$(\Delta V_{{\rm dn},\|},\, V_{{\rm dn},g}) = \left[V_{\rm up}(\alpha - \frac{B_{\rm up,tang.}}{B_{\rm dn,tang.}})\right]\left(\left|\frac{B_{{\rm up},n}}{B_{\rm dn,tang.}}\right|,\, 1\right) \tag{B6}$$

It is worth noting that magnetic field ratios in Equation (B6) can be modulated by self-generated magnetic fields and nonstationarity effects at the shock. Panels (a) and (b) in Figure B1 show the components of the magnetic field tangent and normal to the shock surface for the event discussed in the manuscript.

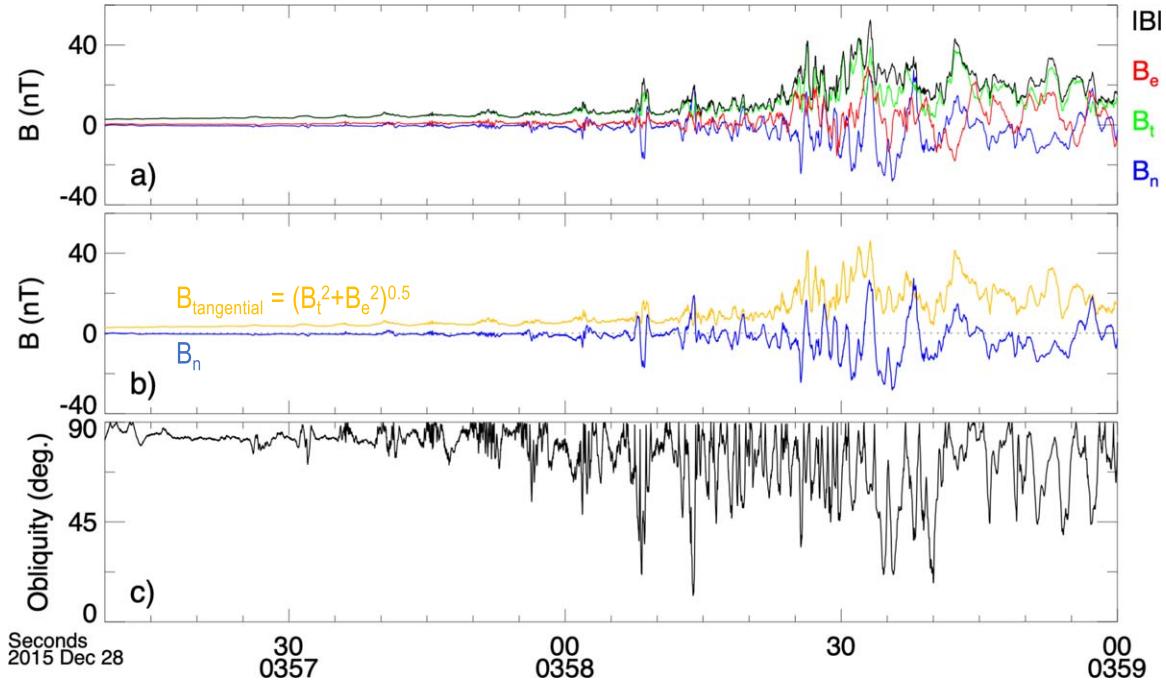

Figure B1. Supporting figure for magnetic field components and local obliquity angle during the shock event on 2015 December 28 at 03:58:24 UT. (a) Magnetic field components interpolated to the center of the four spacecraft tetrahedron and shown in the shock normal coordinates, (b) the total tangential (yellow) and normal (blue) components of the field, (c) the local obliquity angle.

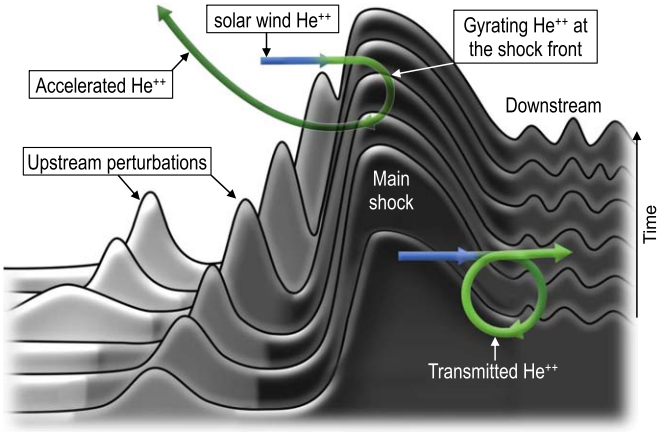

Figure C1. Schematic illustration representing the magnetic field structure and alpha particle dynamics across the shock. The stacked magnetic field profiles (black lines) represent variations in the field strength across the shock front. The amplitude of each peak indicates the relative magnetic field strength at different times and locations. The actual magnetic field vector also changes in direction. Two example trajectories of reflected (top) and transmitted (bottom) solar wind alpha particles are also overplotted to illustrate the ion behaviors. It should be noted that the ion dynamics have a different time dependence than the illustrated magnetic field variations.

Appendix C
Supporting Figures

Figure C1 shows an artistic rendition of the magnetic field across a reforming shock. Figure C2 shows additional data for the event on 2015 December 28, 03:58:24 UT, while Figure C3 shows supporting data for two other events listed in the last two rows of Table 1. For additional details, see the captions.

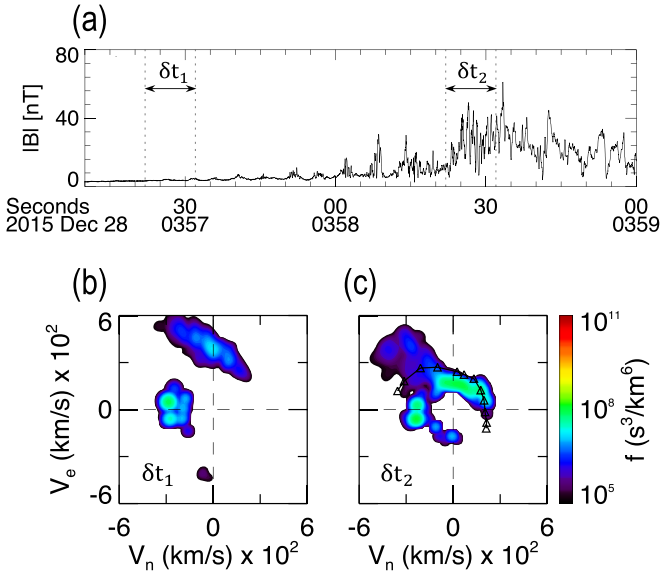

Figure C2. Supporting figure for the shock event on 2015 December 28, 03:58:24 UT. (a) Magnetic field profile across the shock. (b) He^{2+} distribution in the NIF measured upstream of the shock by the HPCA over one measurement cycle (δt_1). In this panel, in addition to the solar wind alpha particle beam, a less intense population in the shape of an arc is observed with velocity component mostly along $+V_e$. These are reflected alpha particles that have been accelerated by the upstream motional electric field and are near the turning point of their gyration. (c) He^{2+} distribution measured across the main shock layer (δt_2). In panel (c), a population of reflected ions with $+V_n$ velocity component propagating away from the shock is also visible. Ion energization along $+V_e$ is not as pronounced as the upstream distribution in panel (b). The black triangle trace, as discussed in Figure 2. (d), is overplotted on this panel for comparison. There is also a more energetic and dispersed ion population (the dark blue patch in the ($-V_n$,$+V_e$) quadrant) that corresponds to returning reflected ions. Ions with the $-V_e$ velocity component can be interpreted as gyrating particles. They can also be due to proton bleedover at low energies (Young et al. 2016; Starkey et al. 2019). HPCA observations confirm the presence of reflected alpha particle upstream of the shock. However, the relatively long measuring cycle of HPCA (10 s) conceals finer details about the reflection mechanism, electric and magnetic field conditions, and subpopulations of ions.

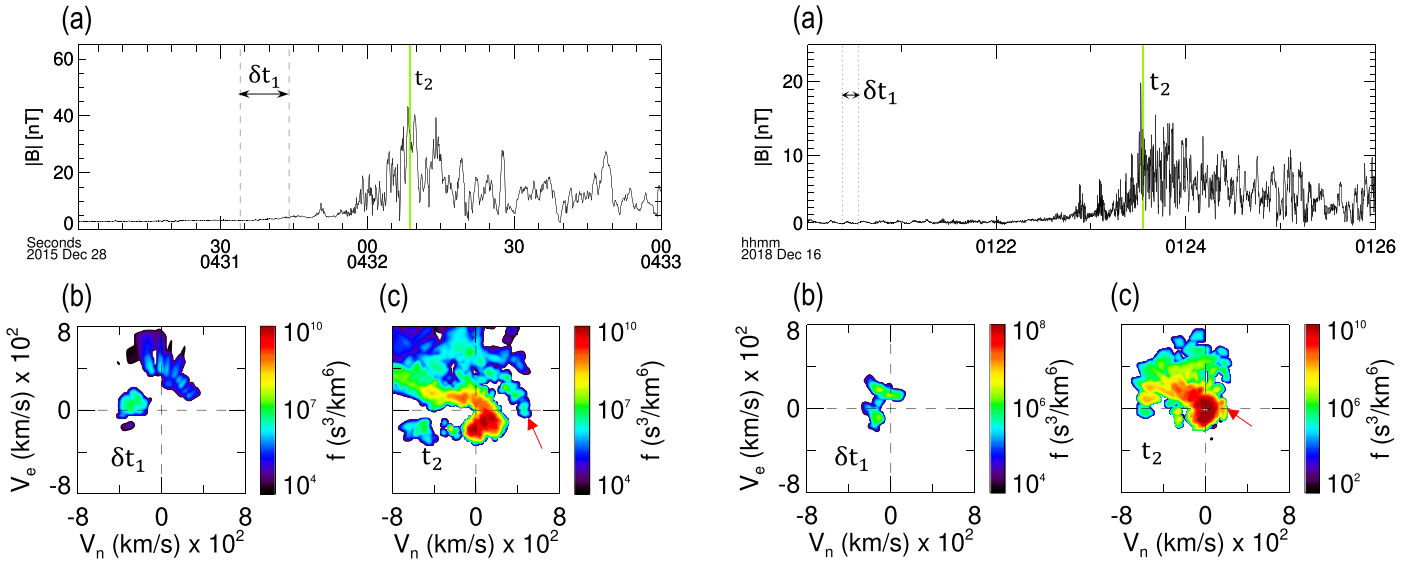

Figure C3. Supporting figures for the shock events on 2015 December 28, 04:32:04 UT (left), and on 2018 December 16, 01:23:32 UT (right) based on MMS3 data. Panels show: (a) magnetic field profile across the shock, (b) HPCA He^{2+} distribution upstream of the shock during δt_1, and (c) FPI ion distribution at the shock front at time highlighted by t_2.

ORCID iDs

Hadi Madanian https://orcid.org/0000-0002-2234-5312
Steven J. Schwartz https://orcid.org/0000-0003-0682-2753
Stephen A. Fuselier https://orcid.org/0000-0003-4101-7901
David Burgess https://orcid.org/0000-0002-8175-9056
Drew L. Turner https://orcid.org/0000-0002-2425-7818
Li-Jen Chen https://orcid.org/0000-0002-4768-189X
Mihir I. Desai https://orcid.org/0000-0002-7318-6008
Michael J. Starkey https://orcid.org/0000-0001-7514-6571

References

Bale, S. D., Mozer, F. S., & Horbury, T. S. 2003, PhRvL, 91, 265004
Bell, A. R. 2004, MNRAS, 353, 550
Broll, J. M., Fuselier, S. A., Trattner, K. J., et al. 2018, GeoRL, 45, 49
Burch, J. L., Moore, T. E., Torbert, R. B., & Giles, B. L. 2016, SSRv, 199, 5
Burgess, D., Hellinger, P., Gingell, I., & Trávníček, P. M. 2016, JPlPh, 82, 905820401
Burgess, D., & Scholer, M. 2013, SSRv, 178, 513
Caprioli, D., Blasi, P., & Amato, E. 2011, APh, 34, 447
Caprioli, D., Pop, A.-R. R., & Spitkovsky, A. 2015, ApJ, 798, L28

Caprioli, D., & Spitkovsky, A. 2014a, ApJ, 794, 46
Caprioli, D., & Spitkovsky, A. 2014b, ApJ, 794, 47
Caprioli, D., Yi, D. T., & Spitkovsky, A. 2017, PhRvL, 119, 171101
Chanteur, G. 1998, in Analysis Methods for Multi-Spacecraft Data, ed. G. Paschmann & P. Daly (Bern: ISSI), 349
De Hoffmann, F., & Teller, E. 1950, PhRv, 80, 692
Eichler, D., & Hainebach, K. 1981, PhRvL, 47, 1560
Ergun, R. E., Tucker, S., Westfall, J., et al. 2016, The Axial Double Probe and Fields Signal Processing for the MMS Mission (Dordrecht: Springer)
Fuselier, S. A., Lennartsson, O. W., Thomsen, M. F., & Russell, C. T. 1990, JGR, 95, 4319
Fuselier, S. A., & Schmidt, W. K. H. 1994, JGR, 99, 11539
Fuselier, S. A., Shelley, E. G., & Klumpar, D. M. 1988, GeoRL, 15, 1333
Fuselier, S. A., Thomsen, M. F., Ipavich, F. M., & Schmidt, W. K. H. 1995, JGR, 100, 17107
Gedalin, M. 2020a, ApJ, 900, 171
Gedalin, M. 2020b, ApJ, 895, 59
Giacalone, J., Armstrong, T. P., & Decker, R. B. 1991, JGR, 96, 3621
Hellinger, P., Trávnícek, P., & Matsumoto, H. 2002, GeoRL, 29, 2234
Hudson, P. D., & Kahn, F. D. 1965, MNRAS, 131, 23
Ipavich, F. M., Gosling, J. T., & Scholer, M. 1984, JGR, 89, 1501
Kasper, J. C., Stevens, M. L., Lazarus, A. J., Steinberg, J. T., & Ogilvie, K. W. 2007, ApJ, 660, 901
Lee, L. C., & Wu, B. H. 2000, ApJ, 535, 1014
Lindqvist, P. A., Olsson, G., Torbert, R. B., et al. 2016, The Spin-Plane Double Probe Electric Field Instrument for MMS (Dordrecht: Springer)
Liu, T. Z., Hao, Y., Wilson, L. B., Turner, D. L., & Zhang, H. 2021, GeoRL, 48, e91184
Madanian, H., Desai, M. I., Schwartz, S. J., et al. 2021, ApJ, 908, 40
Marcowith, A., Bret, A., Bykov, A., et al. 2016, RPPh, 79, 46901
Marcowith, A., Ferrand, G., Grech, M., et al. 2020, LRCA, 6, 1
Meyer, J., Drury, L. O., & Ellison, D. C. 1997, ApJ, 487, 182
Miceli, M., Orlando, S., Burrows, D. N., et al. 2019, NatAs, 3, 236
Paschmann, G., Sckopke, N., Bame, S. J., & Gosling, J. T. 1982, GeoRL, 9, 881
Pollock, C., Moore, T., Jacques, A., et al. 2016, SSRv, 199, 331
Russell, C. T., Anderson, B. J., Baumjohann, W., et al. 2016, The Magnetospheric Multiscale Magnetometers (Dordrecht: Springer)
Russell, C. T., Hoppe, M. M., & Livesey, W. A. 1982, Natur, 296, 45
Schwartz, S. J., & Burgess, D. 1991, GeoRL, 18, 373
Schwartz, S. J., Ergun, R. E., Harald, K., et al. 2021, JGRA, submitted (doi:10.1002/ESSOAR.10506367.2)
Starkey, M. J., Fuselier, S. A., Desai, M. I., et al. 2019, GeoRL, 46, 10735
Sulaiman, A. H., Masters, A., Dougherty, M. K., et al. 2015, PhRvL, 115, 125001
Sundberg, T., Burgess, D., Scholer, M., Masters, A., & Sulaiman, A. H. 2017, ApJ, 836, L4
Yang, Z. W., Lembège, B., & Lu, Q. M. 2011, JGRA, 116, A10202
Young, D. T., Burch, J. L., Gomez, R. G., et al. 2016, Hot Plasma Composition Analyzer for the Magnetospheric Multiscale Mission (Dordrecht: Springer)
Zimbardo, G. 2011, P&SS, 59, 468